Received: 30 January 2025 | Revised: 11 April 2025 | Accepted: 13 May 2025

DOI: 10.1111/jace.20681

Journal of the American Ceramic Society

RESEARCH ARTICLE

Ultrafast development of blue pigment for in situ laser digital coloration in the ceramic industry

Abderrahim Lahlahi-Attalhaoui[1] | **Jaime González Cuadra**[1,2] | **Samuel Porcar García**[1] | **Santiago Luis Toca Valero**[1] | **Diego Fraga Chiva**[3] | **Germán F. de la Fuente**[4] | **Juan Bautista Carda**[1]

[1]Department of Inorganic and Organic Chemistry, Universitat Jaume I, Castellón de la Plana, Spain

[2]Department of Materials and Ceramic Engineering/CICECO-Aveiro Institute of Materials, Portugal, University of Aveiro, Aveiro, Portugal

[3]Ceramic Technology Department, Escola Superior de Ceràmica de L'Alcora (ESCAL-ISEACV), L'Alcora, Spain

[4]Instituto de Nanociencia y Materiales de Aragón (CSIC-Universidad de Zaragoza), Zaragoza, Spain

Correspondence
Juan Bautista Carda, Department of Inorganic and Organic Chemistry, Universitat Jaume I, Avenida Vicent Sos Baynat, s/n, 12071, Castellón de la Plana, Spain.
Email: carda@uji.es

Abstract

This study presents a fast and simple method for digital ceramic coloration using inkjet printing, eliminating the need for traditional precalcined pigments. This innovative approach represents a breakthrough in ceramic decoration technology, and introduces a previously unexplored methodology. In this work, $CoAl_2O_4$ spinel, a pigment commonly used in industrial contexts, is synthesized through laser zone melting (LZM) by applying pulsed laser radiation at 1064 nm. A standardized methodology to optimize pigment quality is developed, based on laser parameters such as pulse width, frequency, speed, power, and line spacing. Scanning electron microscopy (SEM) is used to determine the optimal laser conditions for obtaining a continuous, defect-free coating, showing that the embedded particles on the surface exhibit a nearly spherical morphology with diameters below 100 nm. The sample with the highest surface quality is further analyzed structurally and optically. X-ray diffraction (XRD) confirms the presence of a pure spinel phase without secondary phases, along with a vitreous phase due to pigment embedding. Fourier-transform infrared spectroscopy (FTIR) and Raman spectroscopy reveal the characteristic vibrational bands of a normal spinel structure. The intense blue color is confirmed by strong absorption at 560 nm in ultraviolet–visible (UV–Vis) spectroscopy, as well as b^* and Δb^* values of 29 and 1.58, respectively, compared to the traditional pigment. This synthesis approach significantly enhances digital ceramic coloration compared to other methods evaluated in this study, offering a scalable, flexible, and more efficient alternative suitable for industrial-scale production.

KEYWORDS
inkjet printing, in situ color development, laser-activated blue inks, rapid synthesis, spinel structure

1 | INTRODUCTION

Cobalt aluminate ($CoAl_2O_4$) is a well-known pigment in the ceramic industry because of its bright blue color and its excellent stability in varying light and weather conditions.[1] These pigments, known as spinels, have a crystalline structure in which cobalt ions (Co^{2+}) are located in tetrahedral sites and aluminum ions (Al^{3+}) in octahedral positions.[2,3] Because of its outstanding optical and physical properties, $CoAl_2O_4$ is a popular choice for many industrial applications, especially in ceramics, where its color and heat resistance are highly valued.[4]

$CoAl_2O_4$ pigments have traditionally been synthesized through solid-state reactions,[5] a method in which the particle size of the precursors has a significant impact on the final result. This approach has limitations, such as uneven particle size distribution, high levels of impurities, and the need for extremely high temperatures, typically above 1200°C for 120 min. These conditions not only increase energy consumption but can also negatively affect the optical performance of the pigment. The influence of particle size in these processes has been widely documented in the following studies[6–8]: Wet chemical methods have been developed in response to these challenges. For example, in one study,[9] blue pigments were synthesized by aerosol pyrolysis at 600°C, followed by annealing at 1100°C, a lower temperature than in the traditional solid-state method. Another example reduced calcination times and temperatures, synthesizing blue pigment at 1200°C in 60 min.[4] More recently, microwave-assisted solid-state reactions have been explored,[10] achieving spinel structures at 750°C with a short calcination time of just 15 min. These techniques enable the production of pigments with finer particle sizes and higher purity levels, resulting in better optical and physical properties. Despite these breakthroughs, the adoption of these methods in the ceramic industry remains limited due to the significant changes they would require in established industrial processes.

At the same time, the emergence of digital decoration techniques such as inkjet printing has transformed pigment application in ceramics.[11] Inkjet printing allows a precise and efficient deposition of pigments onto ceramic substrates. This contactless method uses extremely fine nozzles (ranging from 40 to 100 μm in diameter) to spray ceramic inks containing finely dispersed pigments, enabling the creation of high-resolution detailed images or decorations.[12,13] However, preparing pigments for these inks presents a significant challenge, as the intensive grinding required to adjust particle size for the printheads can reduce color performance and alter the pigments' physical behavior.[13]

New strategies must be developed to address the challenges of energy consumption, product quality, and carbon footprint reduction in pigment synthesis and application. A promising technology for revolutionizing the ceramic pigment industry is laser zone melting (LZM). While its use in this domain is relatively recent, the application of laser radiation in solid-state synthesis has been studied for several decades.[14]

An early application of laser radiation in the growth of single crystals can be traced back to 1989, when it was used to synthesize rare-earth oxyorthosilicates and hexagonal oxyapatites from polycrystalline precursors.[15] This process employs the photothermal energy from a pulsed laser to drive solid-state reactions, avoiding the need for high temperatures and extensive grinding. Ceramic compounds were subsequently crystallized in situ as coatings using laser radiation.[16] In one study, neodymium aluminate coatings were developed using this technology, permitting precise control of parameters including irradiance, pulse width, frequency, spatial overlap (SO), and scanning speed, all of which directly affect the quality and uniformity of the resulting pigment.[17]

Further investigations have explored other applications of laser technology, including the growth of eutectic crystals of Er^{3+}-doped ZrO_2–CaO, resulting in alternating layers of calcia-stabilized zirconia (CaSZ) and $CaZrO_3$ crystals.[15] Additionally, coatings based on $MTiO_3$-type perovskites (where M is Ca, Sr, or Ba) with dielectric properties have been developed, and layers of rare-earth and aluminum oxides have been studied on Al_2O_3 substrates, using powder mixtures of rare-earth oxides and Al_2O_3.[18] These solid-state processes have yielded well-integrated and mechanically stable coatings. Lasers can also control reaction atmospheres during solid-state synthesis. In another study,[19] a method was developed for the rapid synthesis of highly luminescent, long-lasting phosphors based on $SrAl_2O_4$ doped with Eu^{2+} and Dy^{3+}. High-power CO_2 laser irradiation achieved sufficiently high temperatures to synthesize these materials in a single step at atmospheric pressure, using mixtures of $SrCO_3$, Al_2O_3, Eu_2O_3, and Dy_2O_3 as precursors.

Laser technology offers significant advantages for pigment production, particularly in the context of LZM. This technique permits selective heating and melting of powder particles, providing precise control over the material's properties and structure. Localized melting of particles is achieved by focusing the laser energy on specific areas. The use of pulsed lasers also enables efficient energy transfer and precise control of reaction conditions, reducing energy consumption and improving the homogeneity of the pigments produced.[14]

The objective of this study is to develop a $CoAl_2O_4$ blue pigment, widely used for digital coloration in the ceramic industry, using LZM as a scalable synthesis tool. To achieve this, a standardized methodology is established to analyze how various laser parameters influence pigment quality, specifically examining the effects of pulse duration, pulse repetition frequency, scanning speed, line spacing (hatching), and laser power on pigment properties. The synthesized pigment is also characterized using multiple techniques to assess its properties: scanning electron microscopy (SEM) for surface morphology, energy-dispersive spectroscopy (EDS) for elemental composition, X-ray diffraction (XRD) for crystalline phases, Fourier-transform infrared spectroscopy (FTIR) for chemical bonds, Raman spectroscopy for molecular vibrations, ultraviolet–visible (UV–Vis) absorption for light absorption, and CIE Lab colorimetry for color properties.

2 | EXPERIMENTAL PROCEDURES

2.1 | Materials and methods

The materials used to prepare the photothermally activated cobalt inks included cobalt oxide (III) (Co_2O_3; 98% purity), aluminum oxide (III) (Al_2O_3; 98% purity), both from Merck, ceramic frit (the chemical analyses by X-ray fluorescence [XRF], structural analyses by XRD analysis, and thermal analyses by hot stage microscopy [HSM] are presented in Figure 1), branched polyethyleneimine (C_2H_5N; 97% purity, Thermo Scientific Chemicals) with a medium molecular weight of M_w ~25 000 to form a very stable cross-linked polymer with the metal.[20] Finally, high purity isopropanol (C_3H_8O; 99% purity, Merck) was used as the solvent.

The frit used in the ink was structurally characterized by XRD, carried out with a Bruker-AXS (D4 Endeavor) instrument within the 2θ (°) range of 10–100, using Cu Kα radiation (λ = 1.54050 Å) and a scanning speed of 0.5° 2θ/min. The chemical composition was determined by XRF analysis using a Bruker S4 Pioneer model wavelength-dispersive XRF spectrometer. The characteristic viscosity points of the frit were measured using a hot stage microscope (TA Instruments Under Waters GmbH, ODP868) with a heating rate of 15°C per min.

The microstructural characterization of the pigmented layers obtained after laser treatment under various conditions was performed using a JEOL 7001F model field emission-scanning electron microscope (FE-SEM). An energy-dispersive X-ray spectrometer (EDX) attached to the aforementioned electron microscope was used to confirm the presence of Co and Al on the surface.

The sample obtained under the most optimal conditions was further characterized using a Fourier-transform infrared spectrometer (FT-IR-6200, JASCO), which enabled the measurement of molecular vibrational transitions within a wavenumber range of 7500–375 cm^{-1}, with a maximum resolution of 0.25 cm^{-1}. An NRS-3100 model dispersive Raman spectrometer (JASCO) was equipped with an optical microscope and an air-cooled CCD detector, allowing Raman transition measurements in the range of 100–4000 cm^{-1} with a resolution of 4 cm^{-1}, using two excitation laser sources at 633 and 785 nm. Lastly, a UV–Vis spectrophotometer manufactured by JASCO (model U-560) was used within a wavelength range of 300–800 nm, at a speed of 400 nm/min with an interval of 1 nm. Using this spectrophotometer, the absorption spectrum and the Lab chromatic coordinates were obtained.

A Raycus RFL-P120MX model pulsed fiber laser was used to crystallize the deposited precursor. The laser emits at a fundamental wavelength of 1064 nm. It is based on a fiber resonator that employs master oscillator power amplification (MOPA) technology. This type of laser is notable for its versatility in dynamically adjusting the pulse width, ranging from 10 to 350 ns, and offering a modulable power range from 10 to 120 W, with a peak power of ≤15 kW. The pulse repetition frequencies can be adjusted between 1 and 1000 kHz. The diagram in Figure 2 shows the apparatus employed to carry out the experiments described in this study. It includes a fiber laser resonator (1), a galvanometer scanner with two mirrors that deflect the beam in the x and y direction (2), a conventional lens with a 160 mm focal length which determines the working distance and field (>25 cm^2), as well as the beam displacement speed (10–3000 mm/s). The diameter of the focused beam was determined as 54 μm ($1/e^2$) using the method reported by Liu.[21]

2.2 | Preparation and optimization of ink

The $CoAl_2O_4$ ink was formulated using 0.13 g of Co_2O_3 and 0.11 g of Al_2O_3, representing 27 wt.% and 22 wt.%, respectively. Additionally, 0.24 g of ceramic frit was incorporated, making up 50 wt.%, acting as a vitrifying agent to integrate the pigment into the ceramic substrate. Figure 3 shows a flowchart of the ink preparation process. In the first step, the solid phase representing 40 wt.% of the composition is dispersed in 60 wt.% isopropyl alcohol (IPA), which serves as solvent. One drop of polyethylenimine (PEI) is then added for each milliliter of IPA to form a very stable cross-linked polymer with the metal, modifying the decomposition mechanism of the precursor and adjusting the viscosity of the suspension.[22,23] In the second step,

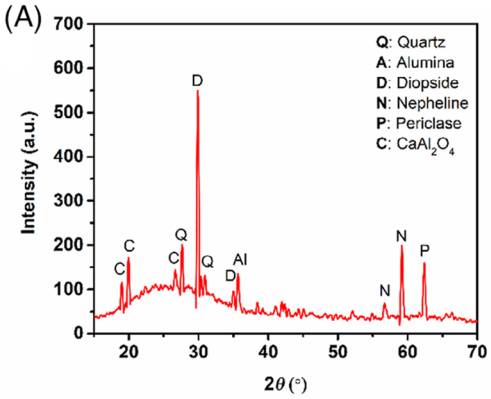

(B)

Oxides	Wt (%)
Na_2O	0 to 18
K_2O	3 to 08
CaO	11 to 98
MgO	1 to 28
ZnO	11 to 7
Al_2O_3	7 to 31
B_2O_3	0 to 37
SiO_2	62 to 26
Fe_2O_3	0 to 12
TiO_2	0 to 03

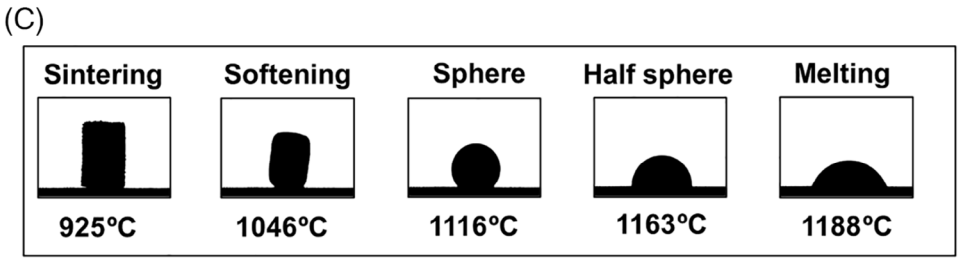

FIGURE 1 Characterization of the ceramic frit used; (A) Structural analysis by X-ray diffraction (XRD), (B) Chemical analysis by X-ray fluorescence (XRF), (C) Thermal analysis by hot stage microscopy (HSM).

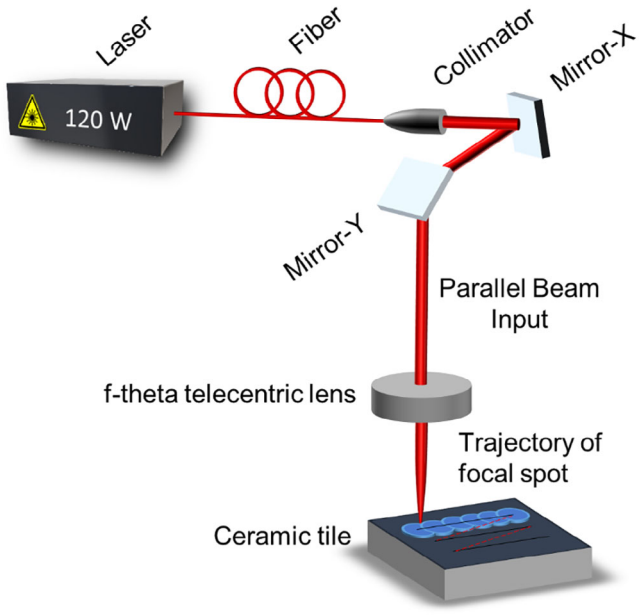

FIGURE 2 Schematic representation of the LASER marking apparatus used in this study, identifying its main components.

a blasé is used to apply the resulting viscous ink onto a ceramic substrate coated with a glaze of the same frit composition. In the third step, the deposited ink is dried under an infrared lamp for 10 min. Finally, in the fourth step, the prepared layer is crystallized using laser irradiation, as detailed in the section below.

2.3 | Methodology for fine-tuning laser parameters

The methodology for optimizing the laser treatment of $CoAl_2O_4$ pigment is shown in Figure 4. This methodology primarily consists of studying three key variables: pulse width (Figure 4A), pulse repetition frequency (Figure 4B), and scanning speed (Figure 4C), in addition to power. When analyzing each variable, a matrix of eight columns and five rows is printed on a sample, resulting in 40 different treatment conditions in which only two variables are compared at a time.

Figure 5 shows the irradiance and SO values analyzed in the methodology described in the figure above. Figure 5A examines how the layer develops as a function of irradiance, and can be varied in two main ways: by adjusting the power levels from 6 to 36 W, and by changing the pulse duration from 50 to 350 ns. The minimum irradiance occurs at a combination of 50 ns and 6 W, while the maximum irradiance is observed at 350 ns and 36 W. All the experiments are conducted at a constant repetition frequency of 1000 kHz to ensure precise control over the influence of each parameter on the final outcome. Figure 5B illustrates the variation of irradiance by adjusting different power levels from 6 to 36 W at various pulse repetition frequencies ranging from 100 to 1000 kHz. The pulse width is kept constant at 50 ns to ensure that the tests are conducted in a comparable manner. Finally, Figure 5C

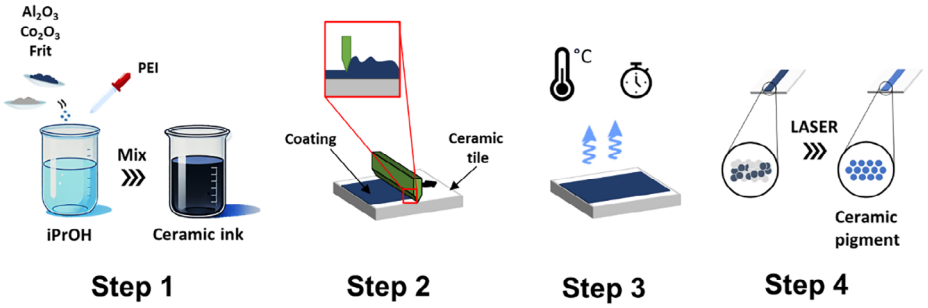

FIGURE 3 Step-by-step diagram of ceramic ink preparation, according to the description provided in the text.

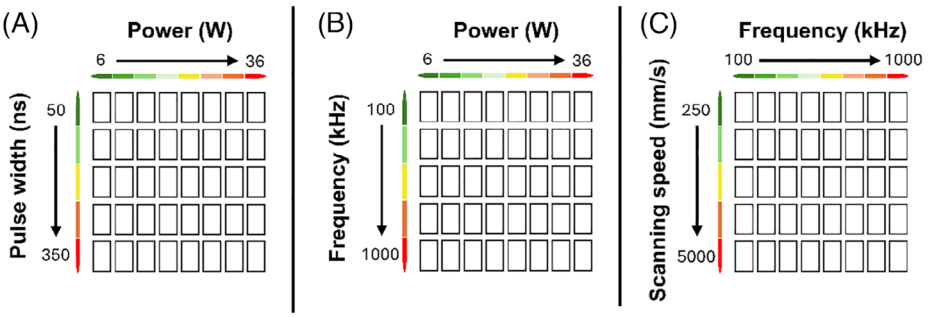

FIGURE 4 Methodology to optimize laser conditions: (A) power versus pulse width, (B) power versus frequency, (C) frequency versus scanning speed.

represents the variation of SO between pulses when varying the repetition frequencies from 100 to 1000 kHz and different beam scanning speeds, ranging from "slow" (250 mm/s) to "fast" (5000 mm/s). In this study, the parameters were kept constant at a power of 19 W, a pulse width of 50 ns, and a line spacing of 1 μm to ensure comparability and facilitate drawing conclusions.

Only the overlap between pulses was considered when calculating the SO, while the overlap between lines was kept constant. The percentage of overlap between laser pulses is calculated using the formula in Equation (1) where the length (L) is measured in millimeters (mm), and the spot diameter ($\varphi_{\text{diameter}}$) is measured in millimeters (mm).

$$\%\ \text{Spacial overlap} = \left(1 - \frac{L}{\varphi_{\text{diameter}}}\right) \times 100 \quad (1)$$

The length (L) is defined as shown below in Equation (2). Beam scanning speed (v), measured in millimeters per second (mm/s), refers to how quickly the laser moves across the material. The pulse period (ω_{pulse}) and pulse duration (τ_{pulse}) are temporal characteristics of the laser pulse, measured in seconds (s). The pulse period represents the total duration of a pulse cycle, while the pulse width indicates the duration of the laser emission.

$$L = v \times \left(\omega_{\text{pulse}} - \tau_{\text{pulse}}\right) \quad (2)$$

The pulse period (ω_{pulse}) is determined by Equation (3) where it is equal to the inverse of the frequency (F_{pulse}):

$$\omega_{\text{pulse}} = \frac{1}{F_{\text{pulse}}} \quad (3)$$

These relationships enable calculation of the overlap, considering the scanning speed, laser spot size, and temporal characteristics of the pulse. A higher percentage of SO indicates greater heat accumulation. Determining the optimal overlap to ensure heat homogeneity on the surface and consequently the continuity and uniformity of the layer is therefore crucial.

3 | RESULTS AND DISCUSSIONS

3.1 | Study of pigment formed in situ and its nanostructural features with electron microscopy

Figure 6 presents five surface micrographs illustrating the effects of different laser treatment power levels on a coating.[24–26] The first micrograph corresponds to the untreated coating, while the other four show the results of applying powers of 6 W, 12 W, 19 W, and 36 W, respectively. The laser pulse parameters, such as duration (50 ns) and frequency (1000 kHz), were kept constant in all

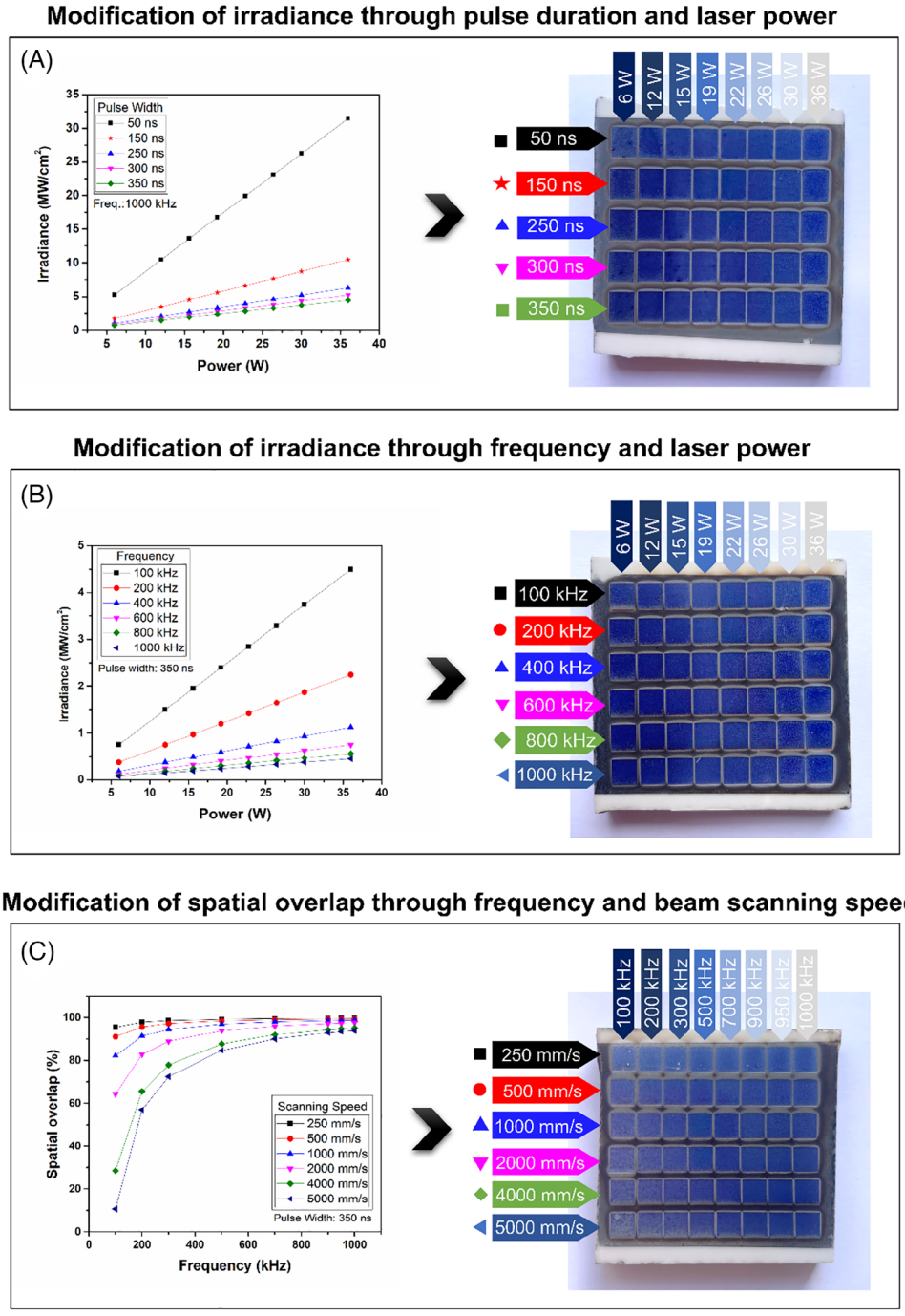

FIGURE 5 Left: Parameter graph; Right: Treated sample. (A) Irradiance variation with power and pulse duration; (B) Irradiance variation with power and frequency; (C) Spatial overlap modulation with scanning speed and frequency.

cases. The calculated irradiances for each power level were 5.24 MW/cm^2, 10.50 MW/cm^2, 16.80 MW/cm^2, and 31.50 MW/cm^2, respectively.[24] Due to the rapid nature of the laser treatment process (which occurs with pulse durations of 50 ns, as specified), direct temperature measurement is challenging. The temperature is therefore estimated indirectly through the behavior of the frit, such as changes in its viscosity and the transition to the molten phase.[27]

The micrographs reveal that at powers of 6 and 12 W, the frit does not fully soften or vitrify in a homogeneous and continuous manner. This is because the irradiances of 5.24 MW/cm^2 and 10.50 MW/cm^2 are insufficient to reduce the frit's viscosity to the point of allowing its transition to a fluid liquid state. According to HSM analysis, this transition occurs at a temperature of 1188°C, which is not reached at these power levels. When the power is increased to 19 W, a continuous layer is observed on the surface, with

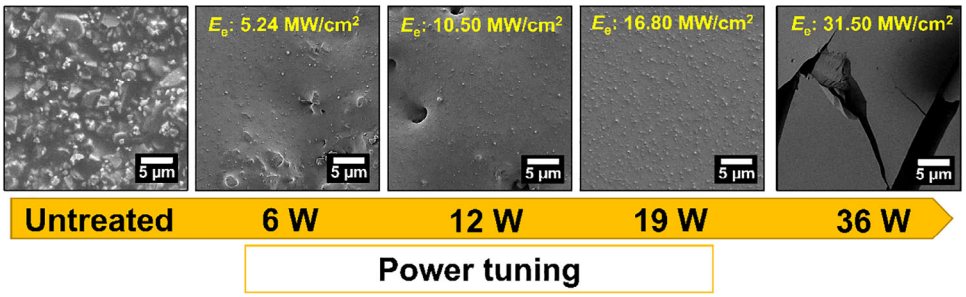

FIGURE 6 Scanning electron microscopy (SEM) micrographs studying layers obtained at different powers.

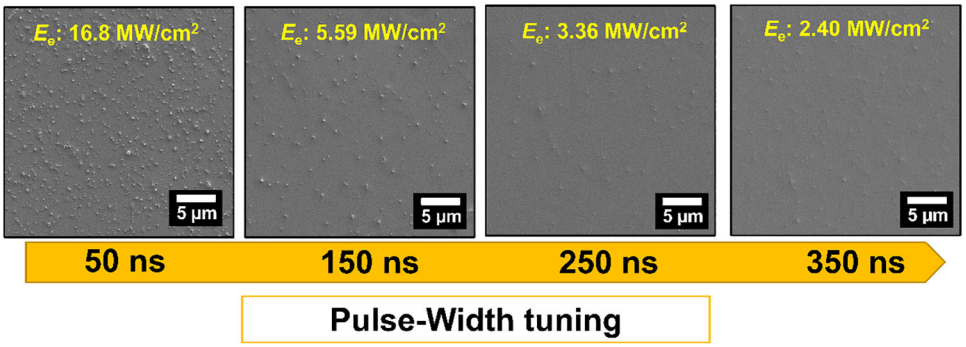

FIGURE 7 Scanning electron microscopy (SEM) micrographs studying layers obtained at different pulse widths.

the presence of $CoAl_2O_4$ pigment crystals, indicating that the optimal power level has been achieved. The stretching of the layer suggests that the frit has melted, exceeding 1188°C. However, when the power is further increased to 36 W, the surface shows significant cracking due to thermomechanical stresses generated during rapid cooling, as evidenced in the rightmost SEM micrograph.[25,26]

Figure 7 shows SEM micrographs of coatings treated at different pulse durations. As we already know that the optimal power is 19 W, as mentioned in the previous section, the power and frequency are kept constant at 1000 kHz, and pulse widths of 50, 150, 250, and 350 ns are studied. The calculated irradiances are 16.8, 5.59, 3.36, and 2.40 MW/cm^2, respectively.[23] The SO level has been kept constant in this series of samples. However, the temporal overlap has increased as the pulse width has been increased. Between 50 and 350 ns, the temporal overlap has changed according to the duration between pulses, from 0.95×10^{-6} s to 0.65×10^{-6} s, respectively. This translates to greater molten layer volume at 350 ns, which allows for liquid-state diffusion of the different pigment elements for nucleation and subsequent crystallization during slower cooling than at 50 ns.[28]

Moreover, at 50 ns pulse durations, the pigment is not completely embedded in the glass matrix, as observed via XRD. However, as the pulse duration increases, the laser's off-time decreases, increasing the molten volume and the interaction time between precursors and the liquid phase of the system. This leads to the formation of a pigment with a smaller particle size that is embedded within the glass, and not observable by XRD.

Figure 8 examines the effect of the repetition frequency, and in this case, samples treated at 100, 200, 600, and 1000 kHz. As we already know that the optimal power is 19 W and 50 ns, these parameters are kept constant, and irradiances of 167.80, 83.88, 27.96, and 16.80 MW/cm^2 are calculated. This parameter influences the amount of accumulated heat and affects the SO of the pulses, which determines the continuity of the layer.[24] The percentage of SO is indicated in the micrographs, and is 64.26%, 82.79%, 95.12%, and 97.59% from the lowest to the highest frequency.

At 100 kHz, the accumulated heat is minimal compared to higher frequencies, resulting in a longer cooling time between pulses. Additionally, at low frequencies, a sufficiently cohesive melting is not achieved due to laser ablation phenomena including fusion, evaporation, sublimation, shock waves that break the grains.[29] This phenomenon results in a heterogeneous layer as the precursors exhibit different levels of stability under the intense laser irradiance of 167.8 MW/cm^2. Furthermore,

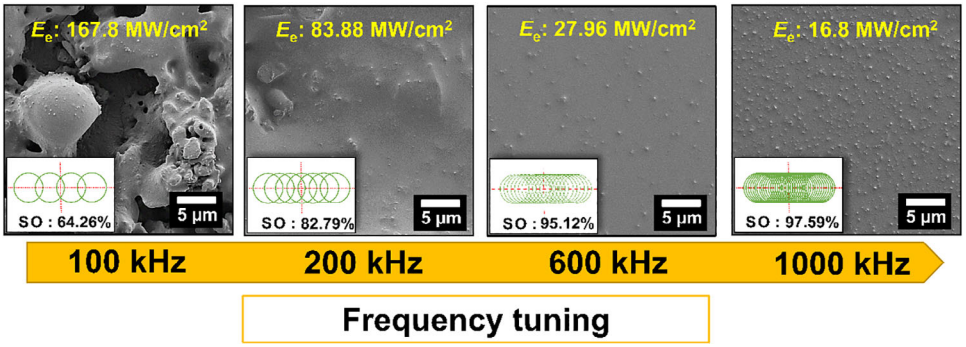

FIGURE 8 Scanning electron microscopy (SEM) micrographs of layers obtained at different frequencies. In the lower left part of each micrograph, the spatial overlap (SO) of the pulses is shown.

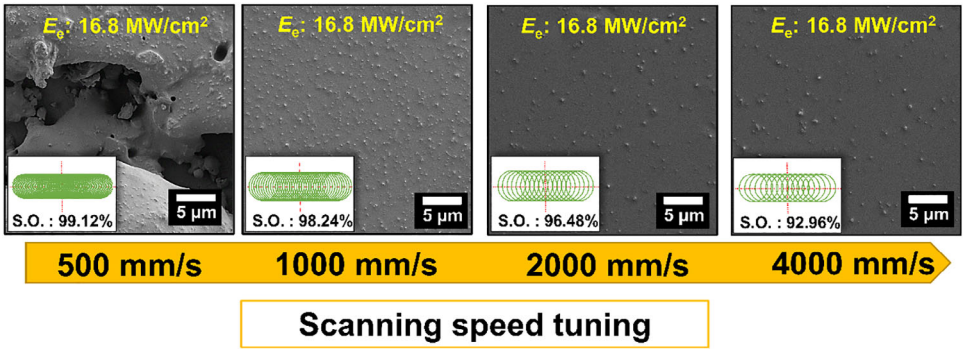

FIGURE 9 Scanning electron microscopy (SEM) micrographs analyzing layers formed at different beam scanning speeds.

this effect is exacerbated due to low SO, which is 64.26%, resulting in areas with little heat accumulation.

As the frequency increases, the layer begins to become more continuous because at higher frequencies, there is a greater accumulation of pulses per unit time, resulting in more uniform treatment with fewer areas of low heat accumulation. The overlap at 1000 kHz is 92.96% and generates a continuous surface as observed in the last micrograph of Figure 8.

Figure 9 examines the influence of scanning speed on the resulting layer. The scanning speeds studied are 500, 1000, 2000, and 4000 mm/s. In this case, the scanning speed is considered not to affect the spot size, thus not affecting the irradiance, and in this series of micrographs, the irradiance is therefore constant at 16.8 MW/cm^2. When the surface is treated at 500 mm/s, the SO is 99.12%, meaning a successive accumulation of heat that exceeds the necessary level for the fusion of the precursors.[30] This leads to ablation phenomena of the frit, resulting in surfaces with defects as observed in the first micrograph. However, when the speed is increased to 1000 mm/s, the overlap decreases to 98.24%, generating a continuous surface without defects. If the speed is increased to 2000 and 4000 mm/s, the result is similar, with overlaps of 96.48% and 92.96%, respectively. In this case, the pulses are spaced further apart spatially, and the heat accumulation is lower, leading to a thinner molten layer and a lower degree of uniformity in the melting.

Figure 10 again shows how the SO between lines affects the resulting layer. Unlike the previous case, this time the SO due to the separation between scanning lines is examined, with samples with separations of 10, 5, 1, and 0.7 µm. Considering that the diameter of the focused spot is 54 µm, according to Liu's theory, overlaps of 81.48%, 85.18%, 98.14%, and 98.70% respectively are calculated.[31] With an overlap of 81.48%, the micrograph shows that there are areas of the surface that do not receive constant or complete irradiation. With greater separation between the scanning lines, not all areas of the surface receive the same amount of laser energy. This leads to less energy accumulation in certain areas, resulting in a discontinuous layer, with poorly covered areas, defects, or even areas with insufficient pigment fusion. However, as the separation is reduced, the layer improves until an overlap of 98.14% is reached, at which point the most optimal layer is obtained. The energy distribution is much more balanced with this level of overlap, favoring the creation of a uniform and continuous layer without voids or defects. When the

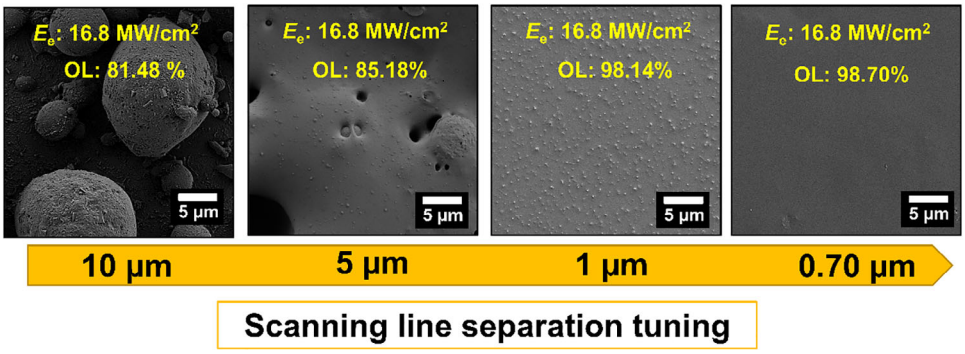

FIGURE 10 Scanning electron microscopy (SEM) micrographs studying layers obtained at different scanning line separations.

separation is reduced to 700 nm and the overlap increased to 98.70%, the accumulated heat causes excessive fusion of the superficial material, creating a structure in a liquid state that remains at a high temperature for too long.[32] This results in the crystals becoming embedded in the glassy matrix.

The micrograph presented in Figure 11 shows the most optimized sample obtained under specific laser treatment conditions, including a power of 19 W, a pulse duration of 50 ns, a frequency of 1000 kHz, a scanning speed of 1000 mm/s, and a line separation of 1 µm. These conditions maximize the treatment's effectiveness, resulting in a ceramic surface that exhibits a homogeneous distribution of spherical and uniform pigment particles, suggesting a controlled synthesis process. Figure 11A shows the spherical morphology of $CoAl_2O_4$ spinel particles are intrinsically related to the pulsed laser treatment characteristics.[33] During the process, the laser generates high-energy pulses that cause rapid heating and cooling of the material. This localized heating creates ideal conditions for the nucleation and growth of particles. In this environment, particles tend to adopt spherical shapes due to the minimization of surface energy, which favors more stable configurations.[34] Additionally, the relatively short pulse duration of 50 ns allows energy to be efficiently transferred to the material without causing significant overheating, which could lead to greater agglomeration or deformation of the particles. The frequency of 1000 kHz and the scanning speed of 1000 mm/s ensure that the treatment is applied uniformly, contributing to the formation of consistently sized particles.

The particle size, analyzed using ImageJ software, is approximately 45 nm on average, with a distribution ranging from 20 to 90 nm, as shown in the graph in Figure 11B. This size distribution is crucial, as greater homogeneity in particle size contributes to a high-quality surface finish. In this synthesis method, the particle size must be measured in situ on the surface because unlike conventional methods that crystallize the powder before application, this technique induces crystallization directly on the surface. As a result, particle formation and growth occur in place, making surface characterization essential for accurately determining the material's final properties.[35]

For this measurement, ImageJ was used with images from Figure 11A. First, the scale was calibrated using a known reference, and image processing techniques were applied to segment the particles and enhance detection. The "Analyze particles" tool was then used to measure parameters such as particle diameter and area. Finally, the data were statistically analyzed to determine the size distribution and its impact on the material's properties. This approach allows for a precise evaluation of the morphology and homogeneity of the surface-formed particles, providing key information for optimizing the synthesis process and improving the optical and mechanical characteristics of the final ceramic material.[13]

Figure 11C presents an EDS spectrum confirming the presence of Co and Al, key elements of the $CoAl_2O_4$ structure, with atomic percentages (%A) of 4.05% and 5.64%, respectively, which are indicative values. Additionally, other elements such as Mg, Si, K, Ca, and Zn are detected, which are part of the glass matrix used in the synthesis, also analyzed by XRF in Figure 1B. The Pt content observed in the spectrum is due to the platinum coating applied to the sample to improve the quality of the images in SEM, preventing charge accumulation on the sample surface and facilitating clearer visualization of its structure.

Figure 12 contains two significant images. Figure 12A shows a backscattered electron SEM micrograph of the optimal sample, designed to emphasize compositional variations more clearly. In this micrograph, the cross-section of the sintered layer is visible, with an approximate thickness of 12.80 µm.

Figure 12B presents the EDS line scanning profile analysis, which provides a measure of the concentration of silicon (Si), cobalt (Co), and aluminum (Al) in the layer. The analysis reveals that the concentration of

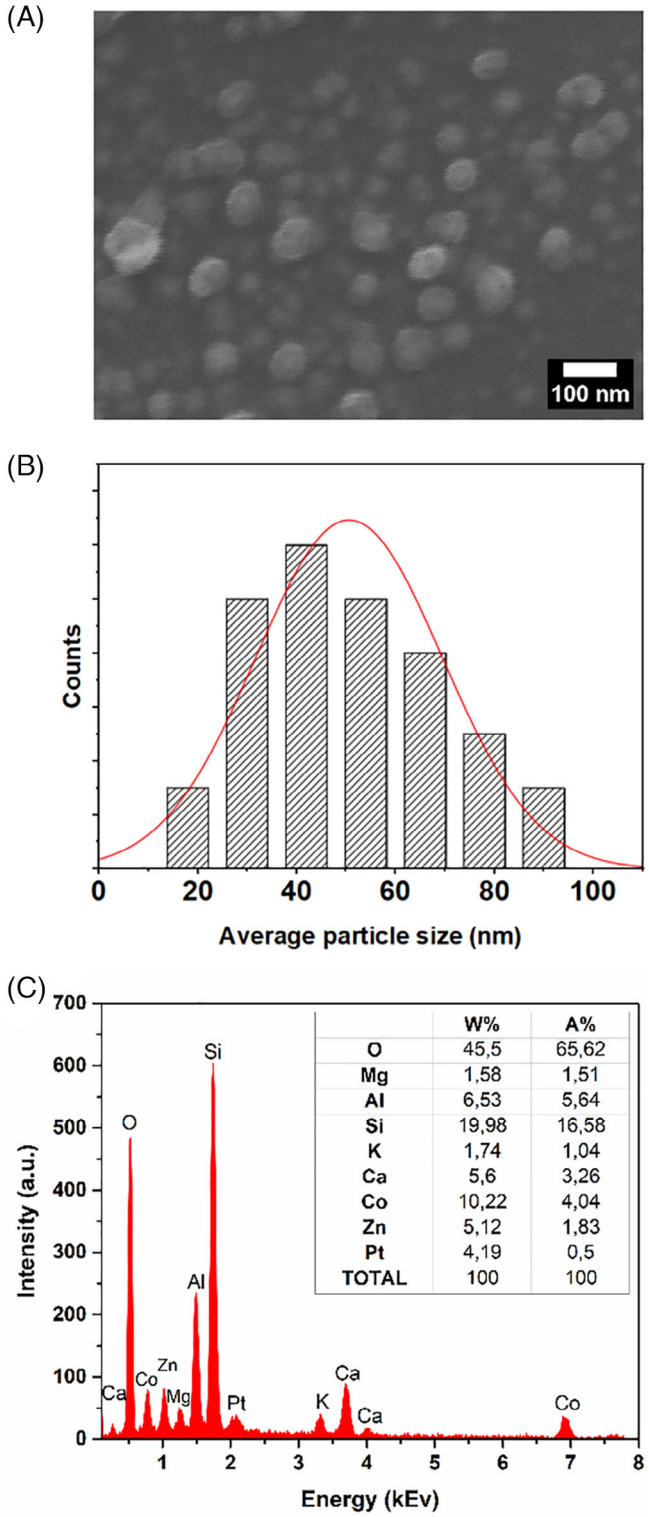

FIGURE 11 Field emission-scanning electron microscope (FE-SEM) microscopy analysis of the surface: (A) Micrograph of the $CoAl_2O_4$ sample after laser treatment; (B) Histogram of the mean particle size distribution; (C) Energy-dispersive spectroscopy (EDS) spectrum.

these elements, expressed as weight percentages, exhibits a gradual variation. The Si content in the substrate is approximately 21%, but it decreases to 9% within the layer, as the layer is composed of frit containing Si along with Co and Al precursors. Cobalt (Co), absent in the ceramic substrate, appears in the treated area of the layer (around 7 μm), where its concentration increases, reaching 15% by weight. Aluminum (Al), already present in the ceramic substrate, shows an increased concentration in the treated region of the layer. This compositional profile confirms the gradual variation in the concentrations of Si, Co, and Al throughout the sintered layer, consistent with the observations from the SEM micrograph in Figure 12A.

3.2 | Structural analysis of the $CoAl_2O_4$ pigment

Figure 13 presents the diffractogram of the sample treated with a laser under optimal conditions: 19 W power, 50 ns pulse duration, 1000 kHz frequency, and 1000 mm/s scanning speed. The crystalline diffraction lines of the sample match the JPCDS reference pattern (01-082-2242) for the spinel $CoAl_2O_4$, identifying the crystalline phase as belonging to the *Fd-3m* (227) space group.[36] The diffraction lines are listed according to their Miller indices in Figure 13, with the (311) peak being the most intense.[37,38] The diffractogram indicates a single-phase spinel structure with no secondary phases. The average crystallite size was calculated using the Scherrer equation (Equation 4), which applies to cubic crystallites in powdered samples:[39]

$$\beta = \frac{K\lambda}{D_{hkl}\cos\theta} \tag{4}$$

The symbol λ denotes the wavelength of the X-ray source, and in this case, λ is equal to 1.5406 μm for the Cu source. Additionally, θ represents the Bragg angle of the diffraction line. The variable D_{hkl} represents the crystallite size, while *hkl* denotes the Miller index, which measures the direction perpendicular to the planes. Furthermore, β_{hkl} refers to the full width at half maximum (FWHM) of the *hkl* plane, measured in radians. The crystallite shape factor, denoted as *K*, is influenced by both instrumental and noninstrumental factors. However, the commonly accepted numerical value for *K* is 0.89 for spherical shapes. The lattice parameter was calculated based on the primary diffraction lines of the cubic spinel structure, and specifically the (111), (220), and (311) lines.

The lattice parameters (h, k, l) for each composition were determined using the following formula:

$$a = d\sqrt{h^2 + k^2 + l^2} \tag{5}$$

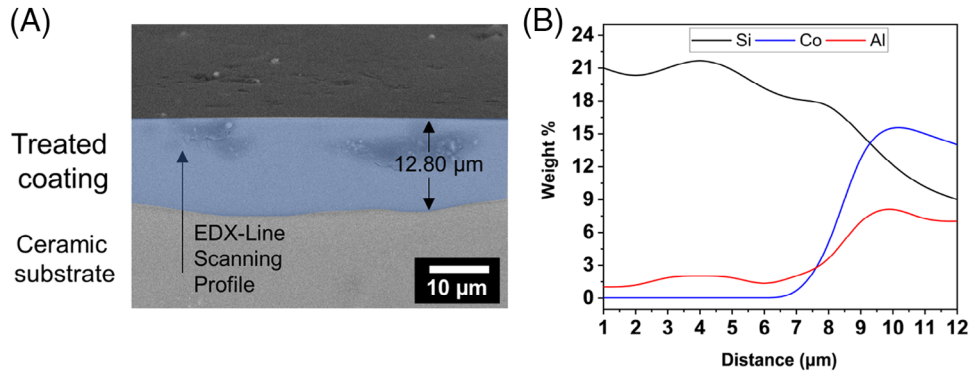

FIGURE 12 Field emission-scanning electron microscope (FE-SEM) analysis of the sample section. (A) shows a micrograph of the layer section as well as a linear scan energy-dispersive X-ray spectrometer (EDX) profile. (B) shows a graph representing the weight % of the elements Si, Co, and Al present in the layer according to the plotted profile line.

TABLE 1 X-ray diffraction (XRD) crystal structure study of the optimized sample synthesized in situ by laser compared to literature data of samples synthesized by other methods.

Sample	Crystallite size (nm)	Lattice parameter (Å)	X-ray density $\rho_x \left(\frac{g}{cc}\right)$	Refs.
In situ laser (this study)	60.24	7.84	4.88	
Solution combustion	22.60	8.10	4.42	42
Nitrate route	285.00	8.11	4.40	43
Sol–gel	27.19	8.13	4.37	44

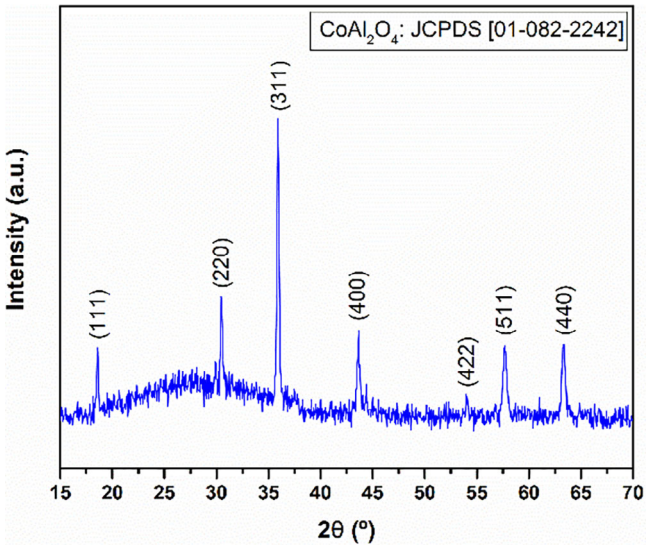

FIGURE 13 Diffractogram of the $CoAl_2O_4$ sample obtained after in situ laser irradiation.

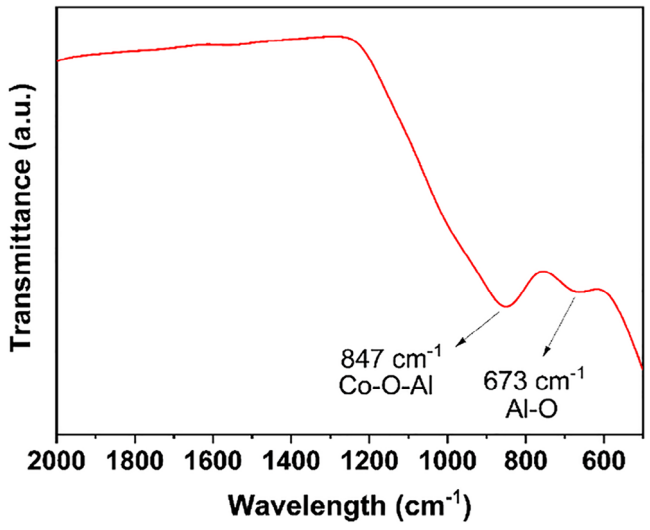

FIGURE 14 Fourier-transform infrared spectroscopy (FTIR) spectrum of optimum sample of $CoAl_2O_4$ prepared in situ by laser.

where (h, k, l) are the Miller indices. The experimental results indicate that the lattice parameters for the sample are 7.84 Å. The formula used to determine the X-ray density is: $\rho_x = \frac{8M}{N\,a^3}$.[40,41] The relationship between the molecular weight of the sample (ρ_m), Avogadro's number (N), the lattice parameter (a), and the molecular weight of the sample determines the measured density. Table 1 provides a list of all the parameters determined using the XRD pattern, compared with the parameters obtained in this work.

The FTIR spectrum (Figure 14) reveals two main overlapping bands that correspond to the molecular vibrations

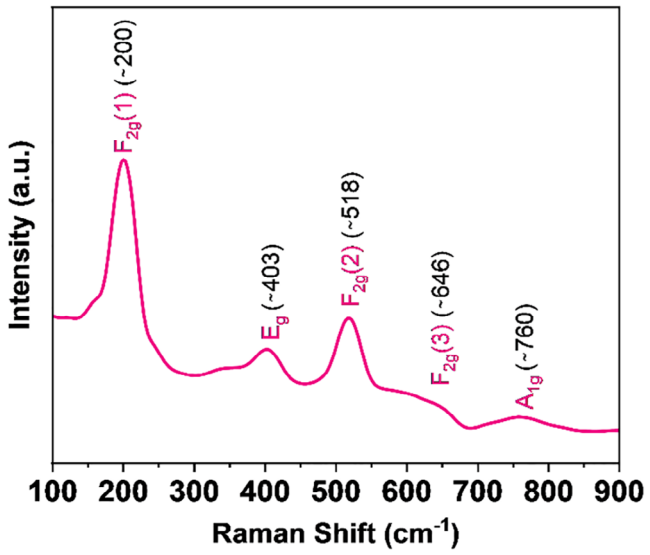

FIGURE 15 Raman spectra of optimum $CoAl_2O_4$ sample prepared in situ by laser.

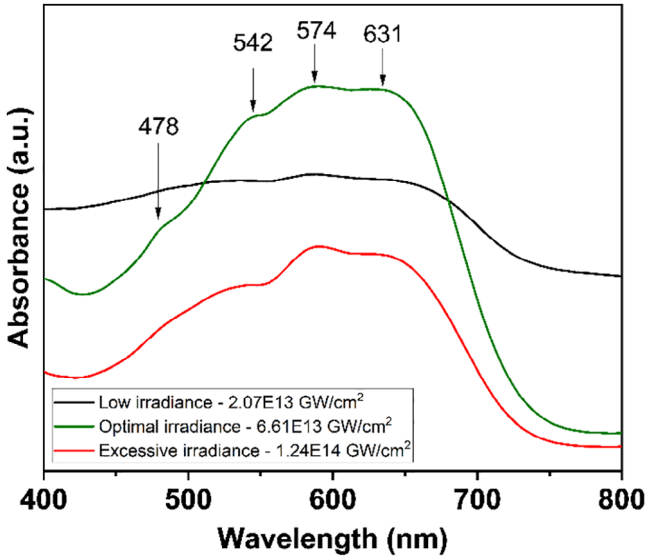

FIGURE 16 Ultraviolet–visible (UV–Vis) absorption spectrum of the laser-treated sample at low, optimum, and high irradiances.

of the transition metal–oxygen bonds. In the case of $CoAl_2O_4$ the spinel's absorption band observed between 640 and 760 cm^{-1} is attributed to Al–O vibrations within the octahedral AlO_6 configuration. If a band appeared at around 800 cm^{-1}, it would be linked to tetrahedral Al–O vibrations (AlO_4). Furthermore, the Co–O–Al interactions exhibit frequencies at around 850 cm^{-1}. As a normal spinel, $CoAl_2O_4$ demonstrates a preference for aluminum ions occupying octahedral sites, while cobalt ions favor tetrahedral sites.[45]

Raman spectroscopy was employed to confirm the spinel structure. As shown in Figure 15, the analysis of the optimal sample reveals five distinct Raman-active peaks. In the case of spinels, the vibrational modes at each Wyckoff position are described by specific irreducible representations[46,47]:

- Site 8a: F_{1u} (IR) + F_{2g} (R)
- Site 16d: A_{2u} (S) + E_u (S) + F_{2u} (S) + $2F_{1u}$ (IR)
- Site 32e: A_{1g} (R) + A_{2u} (S) + E_u (S) + E_g (R) + $2F_{2g}$ (R) + F_1 (S) + F_{2u} (S) + $2F_{1u}$ (IR)

where (R) and (IR) denote Raman and infrared active vibrational modes, respectively. The other modes marked with (S) are silent. The Raman-active modes of the $CoAl_2O_4$ layer are therefore 3F2g → A1g → Eg. Additionally, the three 3F2g modes are labeled as F2g(1), F2g(2), and F2g(3) based on their wavenumbers.

The F2g(1) mode at 200.86 cm^{-1} is assigned to the translation of the Co/Al–O_4 tetrahedron.[24] The position of the Eg mode has been reported as having a reasonable correlation with the cation radius at the 8a site. The Eg mode at 403.32 cm^{-1} is therefore assigned to the symmetric bending motion of the oxygen atoms within the tetrahedron.[48] The F2g(2) mode at 518.96 cm^{-1} is attributed to the asymmetric stretching vibration of Co/Al–O in tetrahedral sites.[47] The literature is inconsistent regarding the vibrational assignment of the F2g(3) mode at 646.46 cm^{-1}, which has been reported either as the antisymmetric stretching mode of the tetrahedral unit or as an asymmetric bending motion of the oxygen bound to the tetrahedral cation.[48,49] Previous studies of the wavenumber of the A1g mode show that the octahedral cation has a more significant effect than the tetrahedral cation.[50] This supports the assignment of the A1g mode at 760.82 cm^{-1} to the Co/Al–O stretching vibration in the octahedron.

3.3 | Optical properties analysis

Figure 16 shows the UV–Vis spectra of $CoAl_2O_4$ pigments prepared at high irradiances, optimal irradiances, and low irradiances. It is well known that blue pigments can absorb visible light in the range of 500–700 nm. In this figure, the samples exhibit three broad bands at 542, 574, and 631 nm, which are characteristic of the blue color in the visible region. The absorption is attributed to electronic transitions in the $3d^7$ level of Co^{2+} ions in tetrahedral sites. The small bands at 406 and 478 nm are related to the green color, which is attributed to the electronic transition of Co^{3+} in the octahedral structure. The weakness of these bands indicates the presence of fewer octahedral ions, and consequently, a negligible amount of green color in favor

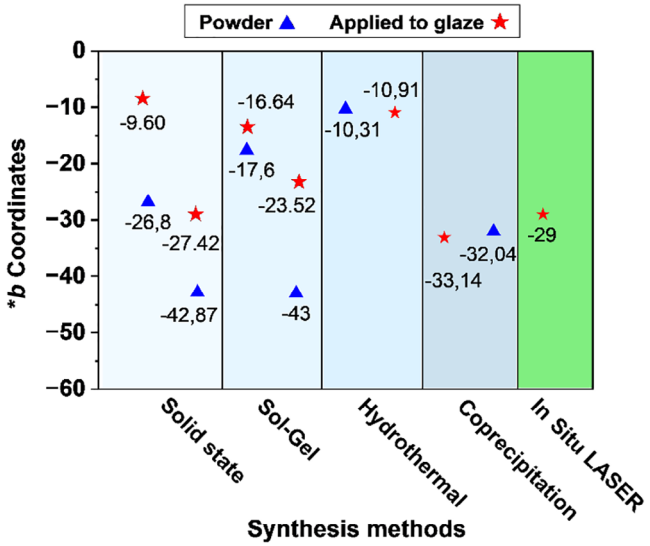

FIGURE 17 Values of the b^* coordinates of various pigments obtained by different synthesis methods compared to the in situ LASER method.

of the blue color.[51] The blue Co^{2+} tetrahedral ions are predominant. The bands at 406 and 478 nm correspond to the ligand-to-metal charge transfer (i.e., from O^{2-} to Co^{2+}) in the tetrahedral site. The existence of these bands is due to the partial oxidation of Co^{2+} ions to Co^{3+} after thermal treatment in the presence of oxygen, leading to the formation of mixed-valence cobalt species (mainly divalent ions with a small amount of trivalent ions) in the thermally treated powders. In this figure, it is evident that at low irradiances, the pigment also absorbs in the 300–500 nm region, so the color is not purely blue. In contrast, at high and optimal irradiances, absorption occurs in the 500–700 nm region, although the absorption is lower at high irradiances.[52]

To analyze color, it is important to understand that it can be represented in different color spaces, with CIELAB being one of the most used due to its perceptual uniformity. In this system, the L^* parameter indicates lightness, ranging from 0 (black) to 100 (white). The a^* value represents the color scale between green (negative) and red (positive), while b^* defines the transition between blue (negative) and yellow (positive).[53–55] Figure 17 presents the b^* coordinate values of different pigments obtained through various synthesis routes, comparing them with those obtained in this study. This graph displays the b^* values of pigments both in powder form and applied to glaze. It is well known that lower b^* values correspond to a more intense blue hue. The solid-state method produces a highly intense blue, with b^* values of −42.87 in powder and −27.42 applied to glaze.[54] In contrast, microwave-assisted calcination results in b^* values of −26.80 in powder and −9.60 applied to glaze.[55]

Alternative methods also achieve intense b^* values, with some even surpassing those obtained with traditional ceramic processes. For instance, in one study,[56] synthesis via sol–gel self-combustion reached a b^* value of −43 in powder and −23.52 applied to glaze. In another study,[57] using the sol–gel autocombustion method, a value of −17.60 was obtained in powder and −16.64 applied to glaze. When hydrothermal methods were used, b^* values of −10.31 were reported in one study,[58] and −10.91 when the hydrothermal reaction was microwave-assisted.[59] For coprecipitation routes, b^* values of −32.04 were achieved, which fell to −33.14 when microwave calcination was applied.[60]

Finally, a b^* value of −29 was obtained by applying the pigment to the glaze using the in situ laser synthesis technique described in this article. This value falls within the range of colors achieved by other methods, even surpassing the traditional method, which reached −27.42. This technique offers significant advantages due to its much more efficient synthesis conditions compared to other approaches.

Table 2 provides a summary of the synthesis characteristics of various blue pigments, organized according to the synthesis method used, pigment type (powder or applied to glaze), and chromatic properties. It includes color coordinates (L, a^*, b^*), as well as ΔE and Δb^* values, which permit the evaluation of deviations compared to a traditional pigment in a vitreous matrix. Additionally, the table lists the treatment temperature and time for each methodology, along with the relevant bibliographic citations.

The in situ laser synthesis method described in this study stands out for its speed and efficiency, with a treatment time of only 30 s for a 4 cm^2 surface. This condition contrasts significantly with the times and temperatures required by other methods presented in the table. For instance, solid-state synthesis methods require temperatures of 1200°C and processing times of up to 240 min, while sol–gel autocombustion techniques operate at temperatures ranging from 900 to 1250°C for at least 60 min. Similarly, although employing lower temperatures (240°C), the hydrothermal method requires extended treatment times of up to 240 min. In comparison, the in situ laser synthesis method not only drastically reduces processing times, but also eliminates the need for high temperatures, representing a significant advantage in terms of energy efficiency and industrial applicability.

Moreover, the color coordinates obtained using this technique show an acceptable deviation for industrial applications, with values of $\Delta E = 13.25$ and $\Delta b^* = 1.58$, indicating a controlled variation in hue within the established parameters.

TABLE 2 Comparative table of color coordinates, temperatures, and synthesis times of pigments with $CoAl_2O_4$ structure synthesized by different methods.

Synthesis method	Pigment type	*L*	*a**	*b**	Δ*E*	Δ*b**	Treatment temperature (°C)	Treatment time (min)	Refs.
In situ laser (this study)	Applied to glaze	31.43	5.76	−29	13.25	1.58	—	0.50	–
Solid-state	Powder	44.35	−13.55	−42.87	18.51	15.45	1200	240	54
Solid-state	Applied to glaze	37.77	−5.77	−27.42	–	–	1200	240	54
Solid-state and microwave treatment	Powder	49.90	−3.70	−26.80	12.32	0.62	1200	120	55
Solid-state and microwave treatment	Applied to glaze	37.7	−4.9	−9.6	17.84	17.82	1200	120	55
Sol–gel autocombustion	Powder	54.20	16.18	−17.60	29.12	9.82	900	120	57
Sol–gel autocombustion	Applied to glaze	34.11	14.91	−16.64	23.61	10.78	900	120	57
Sol–gel self-combustion	Powder	44.39	−8.73	−43	17.18	15.58	1250	60	56
Sol–gel self-combustion	Applied to glaze	46.75	−20.33	−23.52	17.55	3.9	1250	60	56
Hydrothermal	Powder	76.99	−1.24	−10.31	43.03	17.11	240	120	58
Microwave hydrothermal	Applied to glaze	43.63	−6.21	−10.91	17.52	16.51	240	240	59
Coprecipitation and microwave treatment	Applied to glaze	34.98	14.15	−33.14	20.91	5.72	970	40	60
Coprecipitation	Powder	55.29	−8.57	−32.04	18.33	4.62	1000	120	61

4 | CONCLUSIONS

The in situ laser synthesis method presented in this study is an advanced and efficient technology for the production of ceramic pigments in coatings, significantly overcoming the efficiency limitations of traditional methods. This approach permits exceptionally short processing times, achieving results in just 30 s for 4 cm^2 surfaces at a scanning speed of 4000 mm/s, along with a remarkable reduction in energy consumption.

Optimal surface results are obtained with the following parameters: 19 W of power, 50 ns pulse duration, 1000 kHz frequency, 4000 mm/s scanning speed, and 1 μm line spacing, achieving an irradiance of 16.8 MW/cm^2 and a fluence of 0.84 J/cm^2. These conditions facilitate the formation of nearly spherical nanoparticles with sizes below 100 nm, as confirmed by SEM analysis.

XRD analysis validates the formation of a single $CoAl_2O_4$ phase without secondary phases, and also reveals the embedding of the pigment in the vitreous matrix. EDS spectroscopy confirms the incorporation of the pigment into the matrix, detecting the presence of Co and Al, as well as other elements typical of frits such as Mg, Si, K, Ca, and Zn. Raman spectroscopy and FTIR further confirm the formation of a normal spinel structure.

In terms of color, the resulting blue tones show a *b** coordinate value of −29, comparable to pigments synthesized conventionally at 1200°C for 120 min, which show a value of −27.42, with a Δ*b** of 1.58. This demonstrates that the laser synthesis achieves a color quality comparable to traditional methods, but with a much more efficient process.

The morphological, structural, and optical properties obtained confirm that the laser method is a viable alternative for industrial pigment production, offering advantages in speed, energy efficiency, and consistent quality. It aligns with key Sustainable Development Goals (SDGs), including SDG 9 (Industry, Innovation, and Infrastructure), SDG 7 (Affordable and Clean Energy), SDG 12 (Responsible Consumption and Production), and SDG 13 (Climate Action), by improving efficiency, reducing energy use, and promoting sustainable practices. This approach lays the groundwork for future research and industrial applications in laser-based pigment production.

ACKNOWLEDGMENTS

The authors wish to express their gratitude to the Municipal Council of Vila-real for its support through the "Ciutat de Vila-real" Chair in Innovation in Ceramics, and to the Solid State Chemistry Research Group of the Universitat Jaume I for their invaluable contributions. They also extend their thanks to the Generalitat Valenciana for the funding provided through the predoctoral (CIACIF/2022/277), postdoctoral (CIAPOS/2023/425), and international predoctoral mobility (CIBEFP/2024/008) contracts cofinanced by the European Social Fund. The authors are grateful to the Valencian Agency for Research for its support of the project INNEST/2024/420. They also thank the State Research Agency for funding the project TED2021-130963B-C22 (reference: AEI/10.13039/501100011033/European Union NextGenerationEU/PRTR). Additionally, the authors express their gratitude to the Spanish Ministry of Science and Innovation for their support through the project PID2020-116719RB-C43 (MCIN/AEI/10.13039/501100011033). Finally, the authors extend their appreciation to the Universitat Jaume I, particularly the Central Scientific Instrumentation Service, for their technical and scientific support, as well as to the Government of Aragón for their backing through the research group T54_23R.

ORCID

Abderrahim Lahlahi-Attalhaoui https://orcid.org/0009-0004-4380-8824

Jaime González Cuadra https://orcid.org/0000-0003-2655-1524

Samuel Porcar García https://orcid.org/0000-0002-1382-6181

Santiago Luis Toca Valero https://orcid.org/0009-0003-1323-3313

Diego Fraga Chiva https://orcid.org/0000-0003-4820-0135

Germán F. de la Fuente https://orcid.org/0000-0002-0500-1745

Juan Bautista Carda https://orcid.org/0000-0002-4277-6179

REFERENCES

1. Álvarez-Docio CM, Reinosa JJ, del Campo A, Fernández JF. 2D particles forming a nanostructured shell: a step forward cool NIR reflectivity for $CoAl_2O_4$ pigments. Dyes Pigments. 2017;137:1–11. https://doi.org/10.1016/J.DYEPIG.2016.09.061
2. Sickafus KE, Wills JM, and Grimes NW. Structure of spinel. J Am Ceram Soc. 1999;82(12):3279–92. doi: https://doi.org/10.1111/j.1151-2916.1999.tb02241.x
3. Glazer M, Burns G, and Glazer AN. Chapter 2 - Crystal Systems. In: Burns G and Glazer AM, eds. Space groups for solid state scientists. Oxford: Academic Press; pp. 25-44, 2013.
4. Álvarez-Docio CM, Reinosa JJ, Del Campo A, and Fernández JF. Investigation of thermal stability of 2D and 3D $CoAl_2O_4$ particles in core-shell nanostructures by Raman spectroscopy. J Alloys Compd. 2019;779:244–54. https://doi.org/10.1016/J.JALLCOM.2018.11.263
5. Yoneda M, Gotoh K, Nakanishi M, Fujii T, Konishi Y, and Nomura T. Solid-state synthesis and characterization of cobalt blue core-shell pigment particles. J Am Ceram Soc. 2019;102(6):3468–76. doi: https://doi.org/10.1111/jace.16191
6. Andrews AI, Cook RL. Relation of the particle sizes of the frit and color oxides to the color properties of porcelain enamels. J Am Ceram Soc. 1941;24(9):298–310. doi: https://doi.org/10.1111/j.1151-2916.1941.tb14865.x
7. Molinari C, Ardit M, Verucchi D, Tintorri A, Migliori M, Toschi T, et al. Effect of micronisation on colour and optical properties of ceramic colourants for inkjet printing. Ceram Int. 2023;49(17):28465–73. https://doi.org/10.1016/J.CERAMINT.2023.06.101
8. Liu H, Wang Q, Chang Q, Wang C, Wang Y, Wang Y, et al. Relationship between the colour and particle size of the ultrafine V-$ZrSiO_4$ and Pr-$ZrSiO_4$ pigments and their mixture. Mater Res Express. 2019;6(7):075214. https://doi.org/10.1088/2053-1591/ab19e4
9. Ocaña M, Espinós JP, and Carda JB. Synthesis, through pyrolysis of aerosols, of $YIn_{1-x}Mn_xO_3$ blue pigments and their efficiency for colouring glazes. Dyes Pigments. 2011;91(3):501–7. https://doi.org/10.1016/J.DYEPIG.2011.03.009
10. Lahlahi-Attalhaoui A, Cuadra JG, Porcar S, Fraga D, Nebot-Diaz I, Ribeiro RAP, et al. A high-speed method to obtain Ni-Zn ferrite nanoparticles by microwave hydrotalcite decomposition for magnetic applications. J Alloys Compd. 2024;1004:175846. doi: https://doi.org/10.1016/j.jallcom.2024.175846
11. Martin GD, Hutchings IM. Fundamentals of inkjet technology. In: Calvert P, Hutchings IM, eds. Inkjet technology for digital fabrication. Chichester UK: John Wiley & Sons, Ltd; 2012. p. 21–44. Chapter 2. doi: https://doi.org/10.1002/9781118452943.ch2
12. Zhou J, Guo D, Zhang Y, and Rao P. Preparation of submicron-sized $ZnFe_{2-x}Cr_xO_4$ (x = 0.4, 0.8) via a two-step method and evaluation of the corresponding ceramic inks. Mater Chem Phys. 2021;265:124515, https://doi.org/10.1016/J.MATCHEMPHYS.2021.124515
13. Enríquez E, Reinosa JJ, Fuertes V, and Fernández JF. Advances and challenges of ceramic pigments for inkjet printing. Ceram Int. 2022;48(21):31080–101. https://doi.org/10.1016/J.CERAMINT.2022.07.155
14. Stoyanova Lyubenova T, Carda J, and Ocaña M. Nuevos pigmentos cerámicos más respetuosos con el medio ambiente. Editorial Académica Española; 2018.
15. Delafuente G, Black L, Andrauskas D, and Verdun H. Growth of Nd-doped rare earth silicates by the laser floating zone method. Solid State Ion. 1989;32–33(Part 1):494–505. https://doi.org/10.1016/0167-2738(89)90261-0
16. Mandelis A, Vanniasinkam J. Theory of nonradiative decay dynamics in intensely pumped solid-state laser media via laser photothermal diagnostics. J Appl Phys. 1996;80(11):6107–19. https://doi.org/10.1063/1.363685
17. De Francisco I, Bea JA, Vegas A, Carda JB, and De La Fuente GF. In-situ laser synthesis of Nd-Al-O coatings: the role of sublattice cations in eutectic formation. Acta Crystallogr B Struct

Sci Cryst Eng Mater. 2015;71(1):95–111. https://doi.org/10.1107/S2052520615000864
18. Lennikov VV, Pedra JM, Gómez JJ, de la Fuente GF, and Carda JB. In situ synthesis of composite $MTiO_3$-Al_2O_3 coatings via laser zone melting. Solid State Sci. 2007;9(5):404–9. https://doi.org/10.1016/j.solidstatesciences.2007.03.013
19. Aroz R, Lennikov V, Cases R, Sanjuán ML, de la Fuente GF, and Muñoz E. Laser synthesis and luminescence properties of $SrAl_2O_4$:Eu^{2+}, Dy^{3+} phosphors. J Eur Ceram Soc. 2012;32(16):4363–69. https://doi.org/10.1016/j.jeurceramsoc.2012.06.013
20. Ruiz MT, de la Fuente GF, Badía A, Blasco J, Castro M, Sotelo A, et al. Solution-based synthesis routes to $(Bi_{1-x}Pb_x)2Sr_2Ca_2Cu_3O_{10+\delta}$. J Mater Res. 1993;8(6):1268–76. doi: https://doi.org/10.1557/JMR.1993.1268
21. Liu JM. Simple technique for measurements of pulsed gaussian-beam spot sizes. Opt Lett. 1982;7(5):196. [Online]. Available from: https://api.semanticscholar.org/CorpusID:31435075
22. Sotelo A, de la Fuente GF, Lera F, Beltran D, Sapina F, Ibanez R, et al. Novel polymer solution synthesis of the 110 K superconducting phase in the bismuth system. Chem Mater. 1993;5(6):851–56. [Online]. Available from: https://pubs.acs.org/sharingguidelines
23. Sotelo A, Pena JI, Angurel LA, Diez C, Ruiz MT, De La Fuente GF, et al. Synthesis of the $Bi_2Sr_2CaCu_2O_8$ superconductor following a polymer matrix route. J Mater Sci. 1997;32:5679–85.
24. Serdyukov V, Starinskiy S, Malakhov I, Safonov A, and Surtaev A. Laser texturing of silicon surface to enhance nucleate pool boiling heat transfer. Appl Therm Eng. 2021;194:117102. https://doi.org/10.1016/J.APPLTHERMALENG.2021.117102
25. Shukla P, Lawrence J, and Wu H. Fracture toughness of a zirconia engineering ceramic and the effects thereon of surface processing with fibre laser radiation. Proc Inst Mech Eng B J Eng Manuf. 2010;224:1555–69, [Online]. Available from: https://api.semanticscholar.org/CorpusID:62796117
26. Pekkan K, Karasu B. Zircon-free frits suitable for single fast-firing opaque wall tile glazes and their industrial productions. J Eur Ceram Soc. 2009;29(9):1571–78. https://doi.org/10.1016/J.JEURCERAMSOC.2008.10.010
27. Ahn SW, Murphy J, Ramos JA, Wood K, and Beaman JJ. Real-time measurement of temperature for control of laser surface modification process. 2002. [Online]. Available from: https://api.semanticscholar.org/CorpusID:201924310
28. Sitar A, Može M, Crivellari M, Schille J, and Golobič I. Nucleate pool boiling heat transfer on etched and laser structured silicon surfaces. Int J Heat Mass Transf. 2020;147:118956. https://doi.org/10.1016/J.IJHEATMASSTRANSFER.2019.118956
29. Rubahn H-G. Laser applications in surface science and technology. 1st ed., 1 Göttingen, Germany: Wiley-VCH; 1999.
30. Wang X, Zhang Z, Zhao Y, Hu Z, and Li X. Macroscopic morphology and properties of cobalt-based laser cladding layers on rail steel based on pulse shaping. Opt Laser Technol. 2024;168:109940. https://doi.org/10.1016/J.OPTLASTEC.2023.109940
31. Liu HC, Mao XL, Yoo JH, and Russo RE. Early phase laser induced plasma diagnostics and mass removal during single-pulse laser ablation of silicon. Spectrochim Acta Part B At Spectrosc. 1999;54(11):1607–24. https://doi.org/10.1016/S0584-8547(99)00092-0
32. Fiocchi J, Tuissi A, and Biffi CA. Heat treatment of aluminium alloys produced by laser powder bed fusion: a review. Mater Des. 2021;204:109651. https://doi.org/10.1016/J.MATDES.2021.109651
33. Mane ML, Dhage VN, Sundar R, Ranganathan K, Oak SM, Shengule DR, et al. Effects of Nd:YAG laser irradiation on structural, morphological, cation distribution and magnetic properties of nanocrystalline $CoFe_2O_4$. Appl Surf Sci. 2011;257(20):8511–17. https://doi.org/10.1016/J.APSUSC.2011.05.004
34. García-Quiñonez LV, Mendivil-Palma MI, Roy TKD, Castillo-Rodríguez GA, Gómez-Rodríguez C, Fernández-González D, et al. Effects of irradiation energy and nanoparticle concentrations on the structure and morphology of laser sintered magnesia with alumina and iron oxide nanoparticles. Ceram Int. 2020;46(6):7850–60. https://doi.org/10.1016/J.CERAMINT.2019.12.004
35. Latreille P-L, Pazhayattil AB, Turner S, Talwar N. A novel image processing technique for weighted particle size distribution assessment. Drug Dev Ind Pharm. 2024;50(6):550–60. https://doi.org/10.1080/03639045.2024.2358366
36. Ahmed MF, Podder M, Moni MR, Rahman ML, Biswas B, Khanam J, et al. Investigation the effect of calcination heating rate on the structural, morphological, thermal and color properties of nano cobalt aluminate $CoAl_2O_4$. Heliyon. 2025;11(3):e42413, https://doi.org/10.1016/J.HELIYON.2025.E42413
37. Jogi JK, Singhal SK, Jangir R, Dwivedi A, Tanna AR, Singh R, et al. Investigation of the structural and optical properties of zinc ferrite nanoparticles synthesized via a green route. J Electron Mater. 2022;51(10):5482–91. https://doi.org/10.1007/s11664-022-09813-2
38. Chandrani DN, Ghosh S, and Tanna AR. Green synthesis for fabrication of cobalt ferrite nanoparticles with photocatalytic dye degrading potential as a sustainable effluent treatment strategy. J Inorg Organomet Polym Mater. 2024;34(7):3100–3114. https://doi.org/10.1007/s10904-023-02981-6
39. Sahadat Hossain M, Ahmed S. Easy and green synthesis of TiO_2 (anatase and rutile): estimation of crystallite size using Scherrer equation, Williamson-Hall plot, Monshi-Scherrer Model, size-strain plot, Halder-Wagner model. Results Mater. 2023;20:100492. https://doi.org/10.1016/J.RINMA.2023.100492
40. Jagadeesha Angadi V, Manjunatha K, Oliveira MC, Longo E, de Lázaro SR, Ribeiro RAP, et al. Unveiling the shape-selective $CoCr_{2-y}Sc_yO_4$ nanomagnetism. Appl Surf Sci. 2022;574:151555. https://doi.org/10.1016/J.APSUSC.2021.151555
41. Cristina de Oliveira R, Pontes Ribeiro RA, Cruvinel GH, Ciola Amoresi RA, Carvalho MH, Aparecido de Oliveira AJ, et al. Role of surfaces in the magnetic and ozone gas-sensing properties of $ZnFe_2O_4$ nanoparticles: theoretical and experimental insights. ACS Appl Mater Interfaces. 2021;13(3):4605–17. https://doi.org/10.1021/acsami.0c15681
42. Chavarriaga EA, Wermuth TB, Arcaro S, García C, Ramirez MA, Gómez A, et al. One-step synthesis of $CoAl_2O_4$ inorganic pigment by solution combustion: the impact of fuel and ammonium nitrate. Ceram Int. 2024;50(1):45–54. https://doi.org/10.1016/J.CERAMINT.2023.09.205
43. Boudiaf S, Nasrallah N, Mellal M, Belabed C, Belhamdi B, Meziani D, et al. Synthesis and characterization of semiconductor $CoAl_2O_4$ for optical and dielectric studies: application

to photodegradation of organic pollutants under visible light. Optik (Stuttg). 2020;219:165038. https://doi.org/10.1016/J.IJLEO.2020.165038

44. Gao H, Yang H, Wang S, Li D, Wang F, Fang L, et al. A new route for the preparation of $CoAl_2O_4$ nanoblue pigments with high uniformity and its optical properties. J Sol-Gel Sci Technol. 2018;86(1):206–16. https://doi.org/10.1007/s10971-018-4609-y
45. Meyer F, Hempelmann R, Mathur S, and Veith M. Microemulsion mediated sol-gel synthesis of nano-scaled MAl_2O_4 (M = Co, Ni, Cu) spinels from single-source heterobimetallic alkoxide precursors. J Mater Chem. 1999;9(8):1755–63. https://doi.org/10.1039/a900014c
46. White WB, DeAngelis BA. Interpretation of the vibrational spectra of spinels. Spectrochim Acta A. 1967;23(4):985–95. doi: https://doi.org/10.1016/0584-8539(67)80023-0
47. D'Ippolito V, Andreozzi GB, Bersani D, and Lottici PP. Raman fingerprint of chromate, aluminate and ferrite spinels. J Raman Spectrosc. 2015;46(12):1255–64. doi: https://doi.org/10.1002/jrs.4764
48. Shebanova ON, Lazor P. Raman spectroscopic study of magnetite ($FeFe_2O_4$): a new assignment for the vibrational spectrum. J Solid State Chem. 2003;174(2):424–30. doi: https://doi.org/10.1016/S0022-4596(03)00294-9
49. Ding Y, Hu CC, Sheng WQ, Song KX, and Liu B. Crystal structure, microwave dielectric properties, and dielectric resonant antenna studies of novel low-permittivity $CoAl_2O_4$ spinel ceramics. J Mater Sci: Mater Electron. 2021;32(18):22813–21. https://doi.org/10.1007/s10854-021-06760-2
50. Bouchard M, Gambardella A. Raman microscopy study of synthetic cobalt blue spinels used in the field of art. J Raman Spectrosc. 2010;41(11):1477–85. doi: https://doi.org/10.1002/jrs.2645
51. Mindru I, Marinescu G, Gingasu D, Patron L, Ghica C, and Giurginca M. Blue $CoAl_2O_4$ spinel via complexation method. Mater Chem Phys. 2010;122(2–3):491–97. https://doi.org/10.1016/J.MATCHEMPHYS.2010.03.032
52. Peymannia M, Soleimani-Gorgani A, Ghahari M, and Najafi F. Production of a stable and homogeneous colloid dispersion of nano $CoAl_2O_4$ pigment for ceramic ink-jet ink. J Eur Ceram Soc. 2014;34(12):3119–26. https://doi.org/10.1016/J.JEURCERAMSOC.2014.03.022
53. Balakhnina IA, Pushistova AS, Chikishev AY, Kononova EM, Anisimova TI, and Brandt NN. Color trajectories of natural pigments for model fresco samples under heating. Dyes Pigments. 2024;229:112318. https://doi.org/10.1016/J.DYEPIG.2024.112318
54. Melo DMA, Cunha JD, Fernandes JDG, Bernardi MI, Melo MAF, and Martinelli AE. Evaluation of $CoAl_2O_4$ as ceramic pigments. Mater Res Bull. 2003;38(9):1559–64. doi: https://doi.org/10.1016/S0025-5408(03)00136-3
55. Veronesi P, Leonelli C, and Bondioli F. Energy efficiency in the microwave-assisted solid-State synthesis of cobalt aluminate pigment. Technologies (Basel). 2017;5(3):42. https://doi.org/10.3390/technologies5030042
56. Tang Q, Zhu H, Chen C, Wang Y, Zhu Z, Wu J, et al. Preparation and characterization of nanoscale cobalt blue pigment for ceramic inkjet printing by sol-gel self-propagating combustion. Mater Res. 2017;20(5):1340–44. https://doi.org/10.1590/1980-5373-MR-2017-0322
57. Ali AA, Ahmed IS. Sol-gel auto-combustion fabrication and optical properties of cobalt orthosilicate: utilization as coloring agent in polymer and ceramic. Mater Chem Phys. 2019;238:121888. doi: https://doi.org/10.1016/j.matchemphys.2019.121888
58. Obata S, Kato M, Yokoyama H, Iwata Y, Kikumoto M, and Sakurada O. Synthesis of nano $CoAl_2O_4$ pigment for ink-jet printing to decorate porcelain. J Ceram Soc Jpn. 2011;119(1387):208–13, https://doi.org/10.2109/jcersj2.119.208
59. Wang F, Gao P, Liang J, Zhang T, Zhang H, Ding Y, et al. A novel and simple microwave hydrothermal method for preparation of $CoAl_2O_4$/sepiolite nanofibers composite. Ceram Int. 2019;45(18: Part A):24923–26. doi: https://doi.org/10.1016/j.ceramint.2019.08.191
60. Paulo-Redondo G, Nebot-Díaz I. Study of the synthesis variables in the preparation of $CoAl_2O_4$ pigment using microwaves to reduce energetic consumption. Eng. 2023;4(4):2826–39. https://doi.org/10.3390/eng4040159
61. Zhao S, Guo J, Li W, Guo H, and You B. Fabrication of cobalt aluminate nanopigments by coprecipitation method in threonine waterborne solution. Dyes Pigments. 2018;151:130–39. doi: https://doi.org/10.1016/j.dyepig.2017.12.062

How to cite this article: Lahlahi-Attalhaoui A, Cuadra JG, Porcar García S, Toca Valero SL, Fraga Chiva D, de la Fuente GF, et al. Ultrafast development of blue pigment for in situ laser digital coloration in the ceramic industry. J Am Ceram Soc. 2025;e20681. https://doi.org/10.1111/jace.20681